

A sustained high-temperature fusion plasma regime facilitated by fast ions

<https://doi.org/10.1038/s41586-022-05008-1>

Received: 24 September 2021

Accepted: 22 June 2022

Published online: 7 September 2022

 Check for updates

H. Han^{1,9}, S. J. Park^{2,9}, C. Sung³, J. Kang¹, Y. H. Lee^{1,2}, J. Chung¹, T. S. Hahn², B. Kim², J.-K. Park⁴, J. G. Bak¹, M. S. Cha², G. J. Choi², M. J. Choi¹, J. Gwak², S. H. Hahn¹, J. Jang¹, K. C. Lee¹, J. H. Kim¹, S. K. Kim^{4,5}, W. C. Kim¹, J. Ko^{1,6}, W. H. Ko^{1,6}, C. Y. Lee², J. H. Lee^{1,6}, J. H. Lee¹, J. K. Lee^{1,6}, J. P. Lee⁷, K. D. Lee¹, Y. S. Park⁸, J. Seo², S. M. Yang⁴, S. W. Yoon¹ & Y.-S. Na^{2,✉}

Nuclear fusion is one of the most attractive alternatives to carbon-dependent energy sources¹. Harnessing energy from nuclear fusion in a large reactor scale, however, still presents many scientific challenges despite the many years of research and steady advances in magnetic confinement approaches. State-of-the-art magnetic fusion devices cannot yet achieve a sustainable fusion performance, which requires a high temperature above 100 million kelvin and sufficient control of instabilities to ensure steady-state operation on the order of tens of seconds^{2,3}. Here we report experiments at the Korea Superconducting Tokamak Advanced Research⁴ device producing a plasma fusion regime that satisfies most of the above requirements: thanks to abundant fast ions stabilizing the core plasma turbulence, we generate plasmas at a temperature of 100 million kelvin lasting up to 20 seconds without plasma edge instabilities or impurity accumulation. A low plasma density combined with a moderate input power for operation is key to establishing this regime by preserving a high fraction of fast ions. This regime is rarely subject to disruption and can be sustained reliably even without a sophisticated control, and thus represents a promising path towards commercial fusion reactors.

Under the increasing focus on carbon neutrality, nuclear fusion has drawn considerable attention around the world because of its potential to produce massive-scale energy without carbon dioxide or high-level radioactive waste¹. To advance towards economically sustainable power plants with nuclear fusion, it is necessary to maintain plasmas with high fusion performance in steady-state conditions for long pulse durations. To accomplish this, one should produce a plasma with high energy and particle confinement for high fusion performance and a high ion temperature above 100 million kelvin for the high fusion-reaction cross-section. Simultaneously, the plasma should be stable without severe plasma instabilities damaging the device, and should be sustained in steady state by a fully non-inductive current drive without impurity accumulation^{2,3}. Since the 1950s, the tokamak device has been considered and investigated as the first option to confine fusion-grade plasmas, but no tokamak plasma confinement regime realized thus far satisfies all of the above requirements.

In the 1980s, a confinement regime known as high-confinement mode (H-mode)⁵ that relies on confinement improvement at the edge region of the plasma was developed and soon became a mainstream in tokamak research. In H-mode, the plasma turbulence at the edge region is stabilized, resulting in the formation of edge transport barriers (ETBs). H-mode is considered as the reference scenario to produce a fusion power of 500 MW with a fusion gain $Q = 10$ (that is, a fusion power

ten times higher than the input heating power) in the International Thermonuclear Experimental Reactor (ITER)⁶. ITER is the world's largest tokamak, being built in France under a collaboration between China, the European Union, India, Japan, the Republic of Korea, Russia and the USA⁷. However, it has been difficult to achieve high fusion performance and steady-state conditions in standard H-modes although they could enable high confinement and avoid impurity accumulation for a long pulse duration^{8,9}. As a result, various H-modes, such as hybrid mode^{10,11} and high-internal-inductance (I_{ci}) mode¹², based on advanced scenario optimizations, are being developed towards reactor conditions. Still, immanent in any of these H-modes is the large pressure gradient at the edge due to ETBs triggering a problematic edge plasma instability, as these so-called edge-localized modes (ELMs) can severely damage the inner wall of the fusion device¹³. Therefore, vigorous efforts are being made to develop robust methods to control ELMs^{9,14–18}, demanding more complex plasma control systems. As an alternative, internal transport barrier (ITB) discharges, which rely on confinement improvement at the core rather than the edge region owing to core turbulence suppression^{19–21}, have also been introduced^{22–29} and studied. However, these ITB discharges cannot be sustained for a long time, mainly owing to severe instabilities and impurity accumulation in the core region. Other confinement regimes can include some advantages of both ETBs and ITBs as shown in high poloidal beta mode^{22,30} and quiescent double

¹Korea Institute of Fusion Energy, Daejeon, Republic of Korea. ²Department of Nuclear Engineering, Seoul National University, Seoul, Republic of Korea. ³Department of Nuclear and Quantum Engineering, Korea Advanced Institute of Science and Technology, Daejeon, Republic of Korea. ⁴Princeton Plasma Physics Laboratory, Princeton, NJ, USA. ⁵Princeton University, Princeton, NJ, USA. ⁶Department of Accelerator and Nuclear Fusion Physical Engineering, Korean University of Science and Technology, Daejeon, Republic of Korea. ⁷Department of Nuclear Engineering, Hanyang University, Seoul, Republic of Korea. ⁸Department of Applied Physics and Applied Mathematics, Columbia University, New York, NY, USA. ⁹These authors contributed equally: H. Han and S. J. Park. [✉]e-mail: ysna@snu.ac.kr

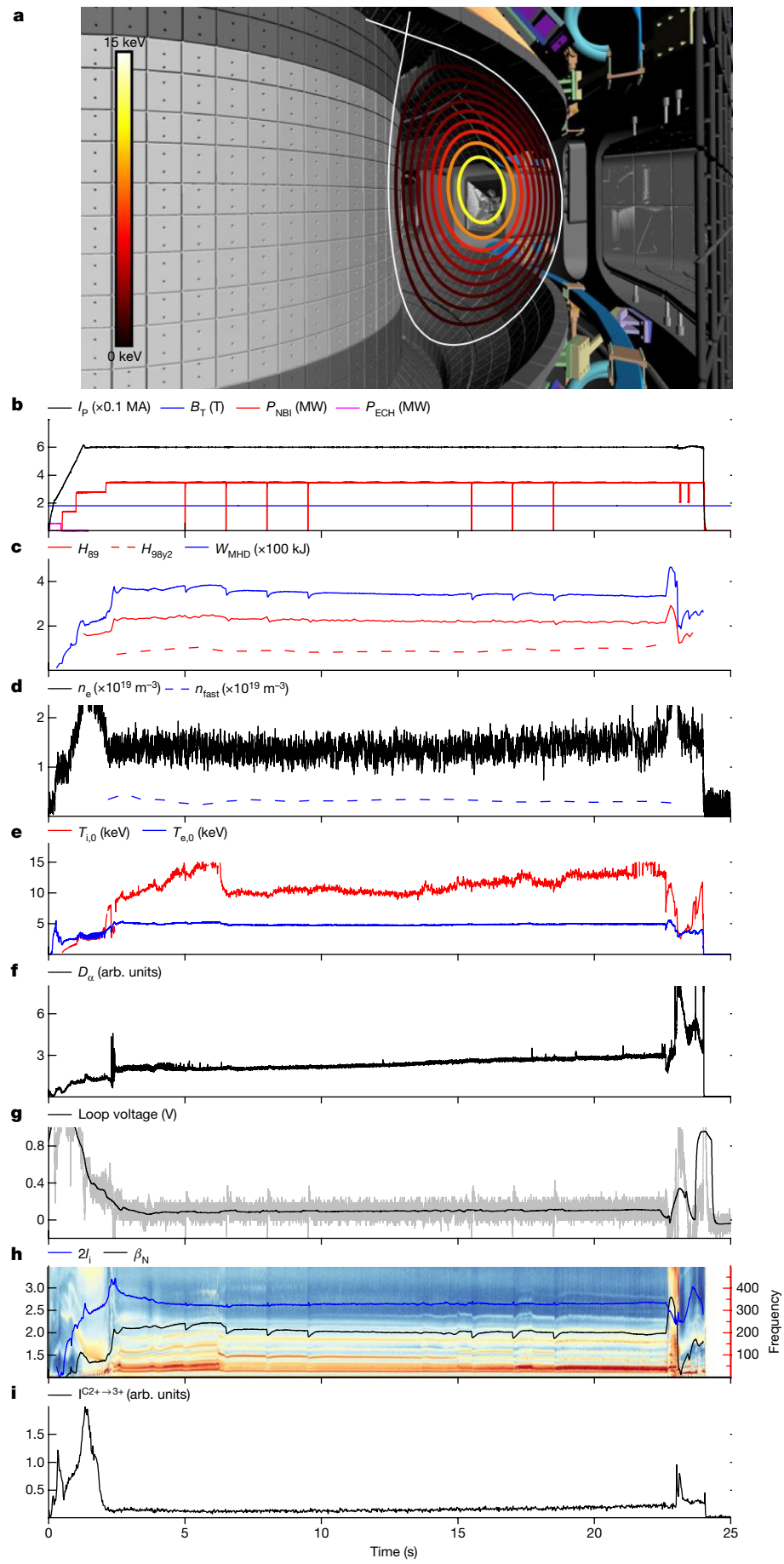
**Fig. 1** | See next page for caption.

Fig. 1 | Tokamak geometry and the parameter evolution of a FIRE mode.

a, The plasma configuration of a FIRE mode in KSTAR. The colour of the lines indicates the ion temperature in kiloelectronvolts, with 10 keV corresponding to ≈ 120 million kelvin. **b–i**, The time evolution of main physics and engineering parameters (shot 25860). **b**, The plasma current (I_p), toroidal magnetic field strength at the magnetic axis (B_T), neutral beam injection power (P_{NBI}) and electron cyclotron resonance heating power (P_{ECH}). **c**, The energy confinement

enhancement factors relative to the ITER89P and the IPB98(y,2) scaling law (H_{89} and H_{98y2}) and stored plasma energy (W_{MHD}). **d**, The line-averaged electron density (n_e) and line-averaged fast-ion density from NUBEAM calculations (n_{fas}). **e**, The central ion and electron temperature ($T_{i,0}$ and $T_{e,0}$). **f**, The D_α emission intensity. **g**, The loop voltage. **h**, The internal inductance (I_i), normalized beta (β_N) and the magnetic fluctuations detected by Mirnov coils. **i**, The carbon line radiation intensity from C^{2+3+} .

barrier mode³¹, but they generally suffer from ELMs, short duration or low non-inductive current drive. Owing to these difficulties, ITER has not yet determined a reliable advanced scenario relevant to a demonstration fusion power plant other than the one for the basic mission.

Here we report a confinement regime recently established in the Korea Superconducting Tokamak Advanced Research (KSTAR)⁴ device, which combines the advantages of H-mode and ITB scenarios and thus can satisfy the requirements described above. This new regime uses an ITB at a low density by avoiding the H-mode transition in the diverted plasma configuration with the unfavourable $B \times \nabla B$ null direction as described in the section entitled Experimental approach in the Methods. As a result, an ion temperature of about 10 keV (≈ 120 million kelvin) has been achieved at the core region and sustained for up to 20 s, a considerable duration (see Fig. 1a and Supplementary Video 1).

Figure 1b–i shows the time evolution of the main physics and engineering parameters for a representative discharge of this regime in KSTAR, illustrating its potential to meet the requirements of commercial fusion reactors. First, the energy confinement is comparable to that of a conventional H-mode. The energy confinement enhancement factors relative to the ITER89P and the IPB98(y,2) scaling law^{32,33}, H_{89} and H_{98y2} , are ≥ 2 and ≈ 1 , respectively (Fig. 1c), similar to $H_{89} \approx 2$ and $H_{98y2} \approx 1$ in typical H-modes. On the other hand, the particle confinement is not enhanced, resulting in a low plasma density (Fig. 1d), which could be the key to prevent ELMs and high impurity accumulation. Second, the plasma temperatures are high, especially the ion temperature, which is important to facilitate the high cross-section for the fusion reaction, above 10 keV (Fig. 1e). Third, D_α signal spikes which mean the spectral line emissions from the ionization of the neutral deuterium are not observed, as shown in Fig. 1f, indicating an absence of ELM activity and their transient heat loads to the wall. As a result, the divertor plate temperature is found to be much lower than that of the standard H-mode operations. That is, this mode can help improve the lifetime of the plasma-facing component of a fusion reactor by preventing the damage induced by heat and particle fluxes. Fourth, almost fully non-inductive current drive is established. As shown in Fig. 1g, the loop voltage, defined as the voltage created by external loop currents concentric with the plasma torus, is sustained at ≈ 0.1 V. This relatively low voltage means that the external inductive flux required for current drive could be minimized. In fact, this new regime is shown to exhibit a low loop voltage of less than 0.1 V, close to 0 V in some cases, which is much lower than that of conventional H-modes. Fifth, this regime is self-sustained for approximately 20 s so that no further delicate feedback control is needed. Note that most of the advanced tokamak operation modes require sophisticated plasma control schemes for pressure or q -profiles³⁴, in which q is the safety factor. Once the plasma enters this new regime, the plasma is kept stationary without severe instabilities such as pressure-driven instabilities commonly found in ITB discharges^{35,36} and/or abrupt plasma disruptions^{37,38}. Note that abrupt plasma disruption is one of the critical issues in fusion plasmas and thus is the highest priority research topic in ITER³⁹. The plasma in this regime has a relatively high internal inductance (I_i) such that it can hold a high plasma pressure normalized to magnetic pressure (β_N) against plasma instabilities⁴⁰. Some instabilities are notably observed in this discharge, as depicted by the Mirnov coil signal (Fig. 1h), which are thought to be related to fast ions. These instabilities can also be identified by the outstanding sound transformed from various diagnostic

signals in Supplementary Video 1. However, their impact on the total stored plasma energy, W_{MHD} , is small, as seen in Fig. 1c, because it is localized within a small volume of the central region of the plasma. Last, Fig. 1i shows that the impurity carbon-III line stays more or less constant during the whole discharge. Generally, there is no substantial degradation in the core electron temperature nor an increase of radiation power observable in this operational mode. All of these findings indicate that notable impurity accumulation is not present and no severe dilution by impurities is foreseen in this confinement regime.

We termed this regime fast-ion-regulated enhancement (FIRE) mode on the basis of the high fraction of fast ions that are noticeable in this regime. Now we address the reasons for the confinement enhancement and the relation to the fast ions. We evaluate the origin of the enhancement of FIRE mode by comparing it with another confinement mode that shows comparable performance. A hybrid mode is selected for this comparison¹⁰, which is based on H-modes but with higher performance as mentioned above. It is an alternative high-performance mode for substituting the H-mode in ITER for engineering tests of reactor-relevant components¹¹ and is considered as a candidate operation mode for DEMO, a demonstration fusion power plant⁴¹. Figure 2 compares the main parameters between the two confinement modes. As shown in Fig. 2a, they exhibit almost identical operating conditions for the plasma current, magnetic field strength and heating power, with the only exception being the plasma configuration. The null magnetic vector potential, where the magnetic field lines intersect in the plasma configuration, is located on the upper region of the plasma (upper single null) in the FIRE mode whereas it is located on the lower region of the plasma (lower single null) in the hybrid mode, as shown in Fig. 2b. Their performance is very similar in the high-heating phase of 5.0 to 8.0 s, as represented by $\beta_N < 2.6$ and $H_{89} < 2.3$. Note that conventional H-modes typically exhibit $\beta_N < 2.0$ and $H_{89} \approx 2.0$ in KSTAR⁴². The triple product ($n_e \tau_{E,th} T_{i,0}$), a figure of merit of the fusion energy gain, is similar between the two modes, $\approx 7 \times 10^{18}$ keV·s·m⁻³ at 5.35 s, with n_e , $\tau_{E,th}$ and $T_{i,0}$ being the line-averaged electron density, thermal energy confinement time and central ion temperature, respectively. Despite their similar performance, the evolutions of the plasma density are very different. This results from different plasma configurations as described in the section entitled Experimental approach in the Methods. The hybrid mode entered the H-mode at approximately 1.8 s, as indicated by the abrupt increases in the performance and density. In contrast, the FIRE mode avoids the H-mode transition over the entire discharge. This is clearly seen in the radial profiles of the temperature, toroidal rotation velocity and density in Fig. 2c. ETBs as an indicator of H-modes are seen in all of the transport channels of the hybrid mode but not in the FIRE mode. Instead, large gradients exist in the core region of the ion temperature in the FIRE mode. As described in the Methods, this large-gradient region exhibits the ITB characteristic, a bifurcation in the energy transport resulting from turbulence stabilization, which was identified along with inverse ion temperature gradient (ITG) lengths above the critical value of ITG turbulence, the value for the ion heat diffusivity lying close to the neoclassical value, an S-curve behaviour of the energy flux and temperature gradient relation, and a reduction of plasma fluctuations in the experiment. In the FIRE mode, both the fast-ion content and the fraction (n_{fas}/n_e) are higher in the core region than those in the hybrid mode, as shown in Fig. 2c. This is consistent with the higher neutron yield, the outcome

Article

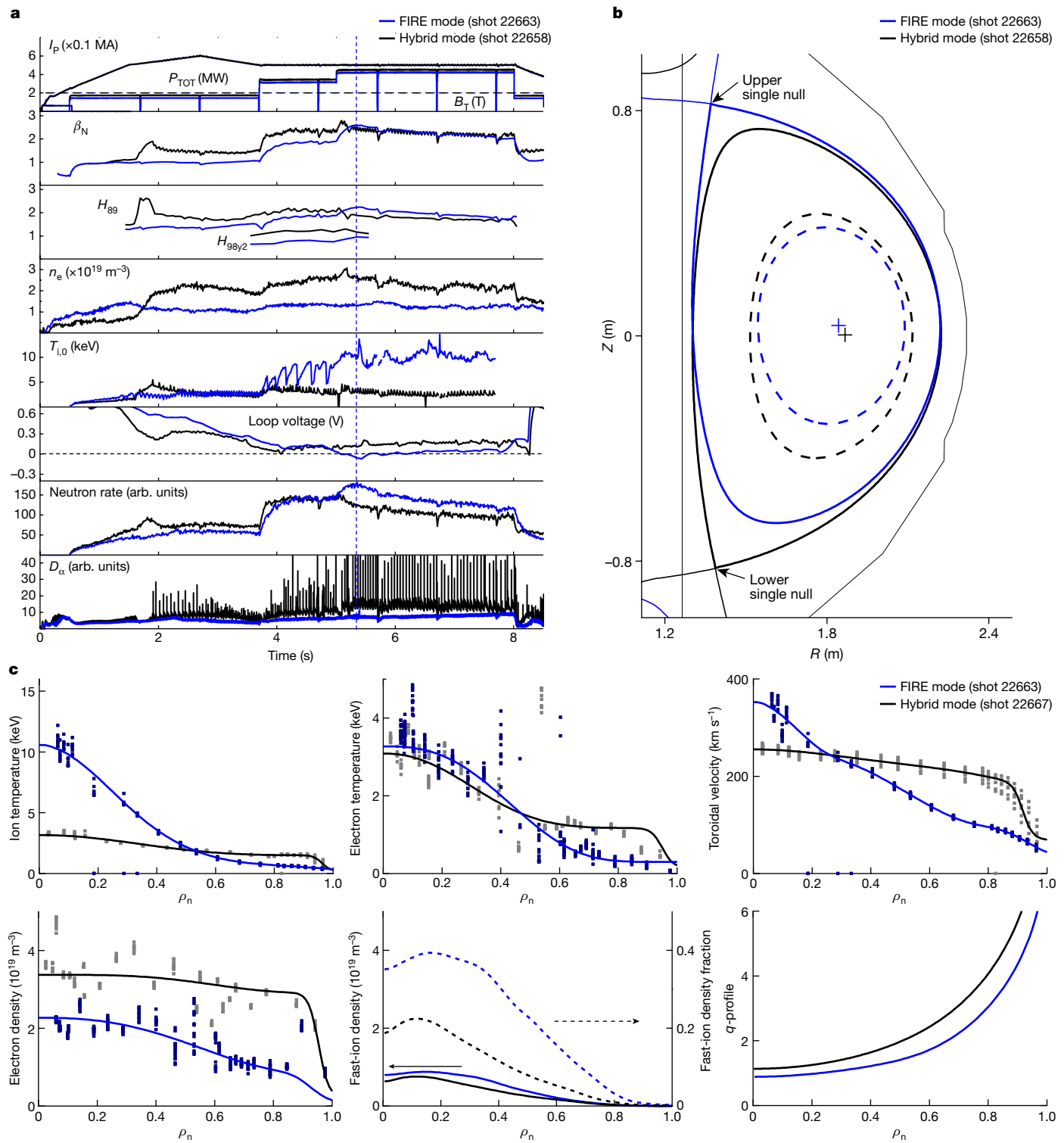


Fig. 2 | Comparison between a FIRE mode and a hybrid mode. **a**, The time evolution of main plasma parameters. I_p (0.1 MA) points to top-line. P_{TOT} (MW) points to stair-shaped line. B_T (T) points to horizontal dashed line. **b**, The plasma configuration at 5.35 s; upper single null in the FIRE mode, lower single null in the hybrid mode. **c**, The ion (top left) and electron (middle left) temperature, toroidal rotation velocity (top right), electron density (bottom left), fast-ion density and fraction (n_{fast}/n_e) (bottom middle) and q -profile

(bottom right) of the FIRE mode (shot 22663 at 5.35 s) and the hybrid mode (shot 22676 at 2.1 s, which is similar discharge to shot 22658) in the normalized toroidal flux, ρ_n . The selected time point, 5.35 s, where the profiles of the FIRE mode were taken, is indicated with the vertical dashed line in **a**. The fast-ion density was calculated by the NUBEAM code. The q -profiles of the FIRE mode and the hybrid mode were calculated from Kinetic-EFIT and MSE-EFIT, respectively.

of fusion reactions by fast ions shown in Fig. 2a. Therefore, one can conjecture that this ITB is strongly correlated with fast ions in the core region of the plasma. As previously reported, fast ions can stabilize

or mitigate microturbulence^{10,43–46} such that the transport of thermal ion energy can be reduced at the core region where the population of fast ions is high.

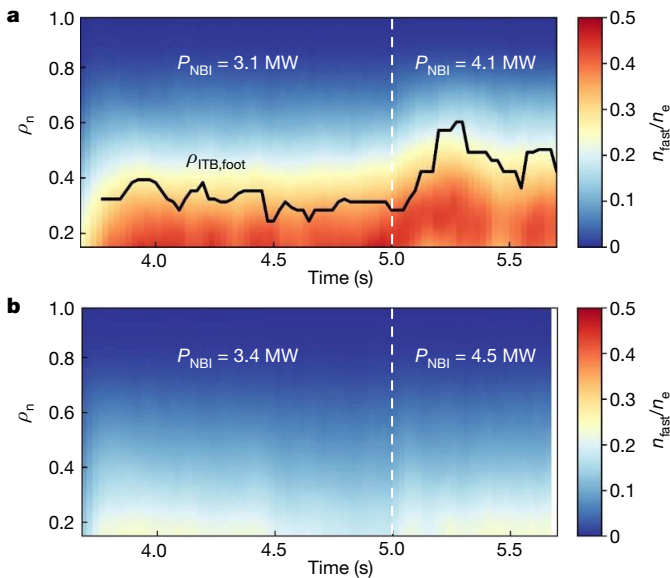


Fig. 3 | The ratio of the fast-ion density to the electron density. **a,b,** The time evolution of the ratio of the fast-ion density to the electron density, n_{fast}/n_e , in a FIRE mode (shot 22663; **a**) and in a hybrid mode (shot 22658; **b**). The fast-ion density was calculated by the NUBEAM code. The characteristic location of core confinement improvement, $\rho_{\text{ITB,foot}}$ (ITB foot location where the second derivative of the ion temperature profile is maximized), is plotted as a black line. The NBI heating power was increased from ≈ 3 MW to ≈ 4 MW at 5.0 s, indicated by the vertical dashed line.

To study the role of fast ions in the confinement enhancement in the FIRE mode, the time evolution of the fast-ion fraction is compared with the location of the ITB, $\rho_{\text{ITB,foot}}$, in Fig. 3a to evaluate the correlation between them. Here $\rho_{\text{ITB,foot}}$ is defined as the position where the second derivative of the ion temperature is maximum^{28,47}. As shown, the ITB seems to be formed at approximately 3.7 s, where the fast-ion fraction is abruptly increased after the second application of neutral beam injection (NBI) heating. The ITB region exists where the fast-ion fraction is high. After applying the third NBI at 5.0 s, the high fast-ion fraction area is expanded up to $\rho_n \approx 0.6$, which is followed by expansion of the ITB, with ρ_n being the normalized toroidal flux depicting a radial position. On the other hand, the fast-ion fraction is lower and there is no ITB in the hybrid mode, as shown in Fig. 3b. This strong correlation between $\rho_{\text{ITB,foot}}$ and the fast-ion fraction indicates that fast ions could play a role in improving the energy confinement through an ITB. As the confinement enhancement is known to be correlated with suppression of turbulence, we next evaluate the effect of fast ions in stabilizing the turbulence using a gyrokinetic simulation code, GKW⁴⁸. Figure 4a,b shows the linear GKW simulation results, in which the linear growth rate (γ) of the ITG turbulence could be lowered while considering the fast-ion effects. That is, ITG, a major contributor to plasma transport, can be stabilized by the fast ions. The stabilization effects of fast ions are achieved through several physics mechanisms. First, the electromagnetic stabilization effect, shown as the difference between the solid and the dashed lines in Fig. 4a, can be reinforced by fast ions. The electromagnetic fluctuations increase the energy needed for the ITG turbulence to grow compared to the electrostatic fluctuations, and the increase in the plasma pressure caused by fast ions can lead to larger electromagnetic fluctuations. Second, the Shafranov shift effect, the so-called α -effect, shown as the difference between the solid and the dashed red lines in Fig. 4b, can also be reinforced by fast ions, with α being $-q^2\beta RVP/P$, in which R is the major radius, and P is the plasma pressure. The Shafranov shift, the outward radial displacement of the centre of flux surfaces, occurs owing to the build-up of the plasma pressure gradient and reduces the vertical drift motion of the plasma driving the

turbulence⁴⁹. The fast ions can enhance the pressure gradient favouring to the Shafranov shift effect. Third, the dilution of the thermal ions and the subsequent reduction in the inverse-normalized density gradient length, R/L_n , in the core region can suppress the ITG turbulence, in which L_n is the density gradient length, $n/\nabla n$. The effect is clearly seen as R/L_n decreases in Fig. 4b, in which the red and the black stars indicate the experimentally relevant reference values with fast ions and assuming no fast ions, respectively. As well as the linear gyrokinetic simulations, nonlinear gyrokinetic simulations have been carried out with CGYRO⁵⁰. Remarkably, as seen in Fig. 4c,d, a substantial reduction of the thermal ion energy flux has occurred when the presence of fast ions is considered. It was reported that the fast-ion stabilization effect also plays a role in the hybrid mode^{10,45}; however, the effect is much lower owing to the smaller fraction of fast ions. As this core improvement in the FIRE mode is comparable to the edge improvement in the hybrid mode, they show similar fusion performances. Owing to the fact that the fast-ion fraction is kept almost constant, the FIRE mode can be sustained for a long duration. This is the result of the balance between the generation and the loss of fast ions. Fast ions are generated mainly from NBI, and there are many loss channels such as thermalization and orbit losses. As some loss terms can be affected by geometric factors, it is worth emphasizing that the extremely low magnetic error field of KSTAR⁵¹ helps to lower this loss rate. From the above, we conjecture that the origin of the high performance of this new regime is mainly attributed to the high fraction of fast ions that stabilize the core turbulence.

We have shown that abundant fast ions exist in the new regime and that they play an important role in confinement enhancement from the experimental observation and the simulation results. However, FIRE may not mean that fast ions fully determine all properties of confinement in the complex fusion plasma system. We still need to find a detailed physical mechanism that can explain how fast ions affect the performance improvement including synergies with other effects such as T_e/T_i , magnetic shear, zonal flow and so on through further nonlinear gyrokinetic simulations and integrated modelling, which remains as future work. In addition, we will pursue an increase of the performance as well as the bootstrap current fraction in the experiment by broadening the ITB and strengthening the I-mode structure at the edge region (Extended Data Fig. 5). Improving wall conditioning by applying boron on the plasma-facing materials (that is, boronization) is also being considered. Further improvement of FIRE modes to realize a longer steady-state operation for several hundred seconds with higher performance is foreseen as one of the promising paths towards a fusion reactor.

Online content

Any methods, additional references, Nature Research reporting summaries, source data, extended data, supplementary information, acknowledgements, peer review information; details of author contributions and competing interests; and statements of data and code availability are available at <https://doi.org/10.1038/s41586-022-05008-1>.

1. Banacloche, S., Gamarra, A. R., Lechon, Y. & Bustreo, C. Socioeconomic and environmental impacts of bringing the sun to earth: a sustainability analysis of a fusion power plant deployment. *Energy* **209**, 118460 (2020).
2. Wesson, J. *Tokamaks* 4th edn, Ch. 1, 2–27 (Oxford Univ. Press, 2011).
3. Wesson, J. *Tokamaks* 4th edn, Ch. 13, 764–767 (Oxford Univ. Press, 2011).
4. Lee, G. S. et al. Design and construction of the KSTAR tokamak. *Nucl. Fusion* **41**, 1515 (2001).
5. Wagner, F. et al. Regime of improved confinement and high beta in neutral-beam-heated divertor discharges of the ASDEX Tokamak. *Phys. Rev. Lett.* **49**, 1408–1412 (1982).
6. Shimada, M. et al. Progress in the ITER physics basis - Chapter 1: Overview and summary. *Nucl. Fusion* **47**, S1–S17 (2007).
7. Barbarino, M. A brief history of nuclear fusion. *Nat. Phys.* **16**, 890–893 (2020).
8. Yoon, S. W. et al. Characteristics of the first H-mode discharges in KSTAR. *Nucl. Fusion* **51**, 113009 (2011).
9. Li, J. et al. A long-pulse high-confinement plasma regime in the Experimental Advanced Superconducting Tokamak. *Nat. Phys.* **9**, 817–821 (2013).
10. Na, Y. S. et al. On hybrid scenarios in KSTAR. *Nucl. Fusion* **60**, 086006 (2020).

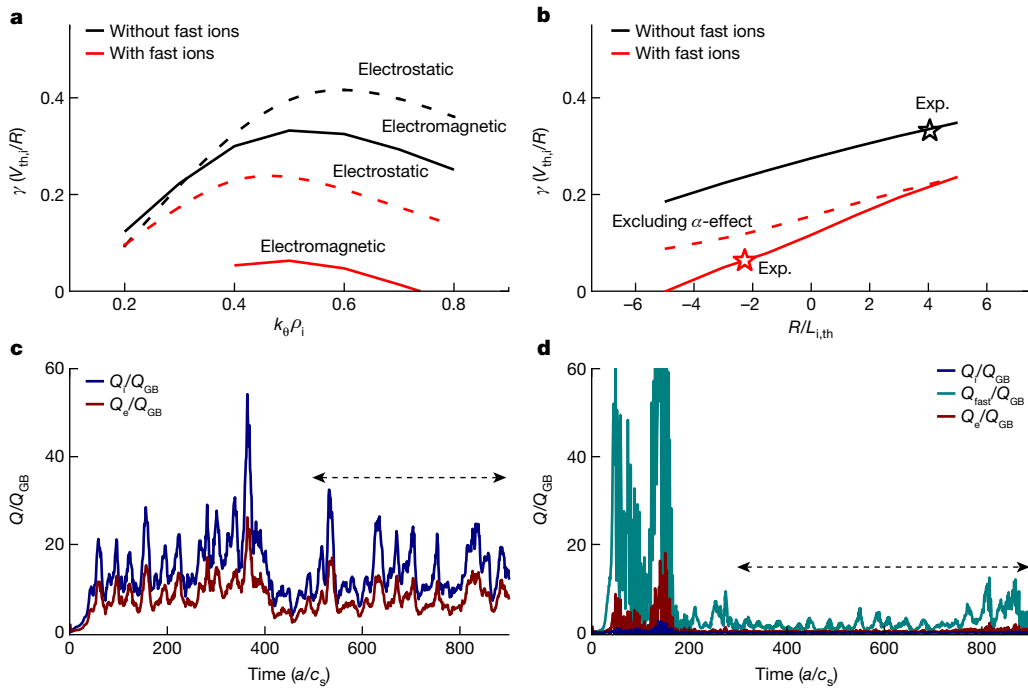


Fig. 4 | The gyrokinetic simulation results of a FIRE mode. **a,b,** The linear simulation results with the GKW code. **a,** The ITG growth rate (γ) versus $k_0 \rho_i$ with electrostatic (dashed lines) and electromagnetic (solid lines) simulations considering (red) and without considering (black) the fast ions. The fast ions are replaced by thermal ions when they are not considered. **b,** The ITG growth rate versus the inverse-normalized thermal ion density gradient length considering (red) and without considering (black) the fast ion for $k_0 \rho_i = 0.5$ exhibiting the maximum growth rate in **a**. Here k_0 and ρ_i are the poloidal wavenumber and the ion gyroradius, respectively. The black and the red star in **b** represent the reference experimental value (Exp.) without and with fast ions, respectively. The thermal ion density gradient is the same as the total ion density gradient for the case without fast ions. Exclusion of the α -effect is compared for the case with the fast ion, shown as the red dashed line in

b, in which α is $-q^2 B R \nabla P / P$. **c,d,** The nonlinear simulation results with the CGYRO code. **c,** The energy fluxes without considering the fast ions versus the simulated time. **d,** The energy fluxes when considering the fast ions versus the simulated time. Each energy flux of thermal ions (Q_i), fast ions (Q_{fast}) and electrons (Q_e) normalized to the gyro-Bohm energy flux ($Q_{GB} = n_e c_s T_e \rho_s^2 / a^2$) is coloured in navy, dark cyan and wine, respectively. Here a is the minor radius, c_s is the sound speed, and ρ_s is the ion sound gyroradius. Note that only the last part of the nonlinear simulation results, indicated by the dashed two-way arrow, should be considered because a certain amount of simulation time is required until the simulated turbulence is saturated by nonlinear effects. Simulations in **a–d** are performed at $\rho_{in} = 0.4$ at 5.35 s in the FIRE mode (shot 22663).

11. Luce, T. C. et al. Development of advanced inductive scenarios for ITER. *Nucl. Fusion* **54**, 013015 (2014).
12. Lao, L. L. et al. High internal inductance improved confinement H-mode discharges obtained with an elongation ramp technique in the DIII-D tokamak. *Phys. Rev. Lett.* **70**, 3435 (1993).
13. Zohm, H. Edge localized modes (ELMs). *Plasma Phys. Control. Fusion* **38**, 105–128 (1996).
14. Lang, P. T. et al. ELM frequency control by continuous small pellet injection in ASDEX Upgrade. *Nucl. Fusion* **43**, 1110–1120 (2003).
15. Degeling, A. W. et al. Magnetic triggering of ELMs in TCV. *Plasma Phys. Control. Fusion* **45**, 1637–1655 (2003).
16. Evans, T. E. et al. Edge stability and transport control with resonant magnetic perturbations in collisionless tokamak plasmas. *Nat. Phys.* **2**, 419–423 (2006).
17. Jeon, Y. M. et al. Suppression of edge localized modes in high-confinement KSTAR plasmas by nonaxisymmetric magnetic perturbations. *Phys. Rev. Lett.* **109**, 035004 (2012).
18. Park, J.-K. et al. 3D field phase-space control in tokamak plasmas. *Nat. Phys.* **14**, 1223–1228 (2018).
19. Burrell, K. H. Effects of $E \times B$ velocity shear and magnetic shear on turbulence and transport in magnetic confinement devices. *Phys. Plasmas* **4**, 1499 (1997).
20. Hahm, T. S. Physics behind transport barrier theory and simulations. *Plasma Phys. Control. Fusion* **44**, A87–A101 (2002).
21. Conway, G. D. et al. Suppression of plasma turbulence during optimized shear configurations in JT. *Phys. Rev. Lett.* **84**, 1463 (2000).
22. Koide, Y. et al. Internal transport barrier on $q=3$ surface and poloidal plasma spin up in JT-60U high- β_p discharges. *Phys. Rev. Lett.* **72**, 3662 (1994).
23. Strachan, J. D. et al. High-temperature plasmas in the Tokamak Fusion Test Reactor. *Phys. Rev. Lett.* **58**, 1004 (1987).
24. Gormezano, C. et al. Internal transport barriers in JET deuterium-tritium plasmas. *Phys. Rev. Lett.* **80**, 5544 (1998).
25. Gruber, O. et al. Steady state H mode and Te-Ti operation with internal transport barriers in ASDEX Upgrade. *Nucl. Fusion* **40**, 1145 (2000).
26. Yu, D. L. et al. Ion internal transport barrier in neutral beam heated plasmas on HL-2A. *Nucl. Fusion* **56**, 056003 (2016).
27. Koide, Y. et al. Characteristic peaked profiles of ion temperature and toroidal rotation velocity in JT-60 hot ion modes. *Nucl. Fusion* **33**, 251 (1993).
28. Chung, J. et al. Formation of the internal transport barrier in KSTAR. *Nucl. Fusion* **58**, 016019 (2018).
29. Chung, J. et al. Sustainable internal transport barrier discharge at KSTAR. *Nucl. Fusion* **61**, 126051 (2021).
30. Garofalo, A. M. et al. Compatibility of internal transport barrier with steady-state operation in the high bootstrap fraction regime on DIII-D. *Nucl. Fusion* **55**, 123025 (2015).
31. Doyle, E. J. et al. The quiescent double barrier regime in the DIII-D tokamak. *Plasma Phys. Control. Fusion* **43**, A95 (2001).
32. Yushmanov, P. N. et al. Scalings for tokamak energy confinement. *Nucl. Fusion* **30**, 1999 (1990).
33. ITER Physics Expert Group on Confinement and Transport et al. Chapter 2: Plasma confinement and transport. *Nucl. Fusion* **39**, 2175 (1999).
34. Crisanti, F. et al. JET quasistationary internal-transport-barrier operation with active control of the pressure profile. *Phys. Rev. Lett.* **88**, 145004 (2002).
35. Manickam, J., Pomphrey, N. & Todd, A. M. M. Ideal MHD stability properties of pressure driven modes in low shear tokamaks. *Nucl. Fusion* **27**, 1461 (1987).
36. Chu, M. S. et al. Resistive interchange modes in negative central shear tokamaks with peaked pressure profiles. *Phys. Rev. Lett.* **77**, 2710 (1996).
37. Okabayashi, M. et al. Mode structure of disruption precursors in TFTR enhanced reversed shear discharges. *Nucl. Fusion* **38**, 1149 (1998).
38. de Vries, P. C. et al. Survey of disruption causes at JET. *Nucl. Fusion* **51**, 053018 (2011).
39. *ITER Research Plan within the Staged Approach* ITER Technical Report ITR-18-003 (ITER, 2018).
40. Strait, E. J. Stability of high beta tokamak plasmas. *Phys. Plasmas* **1**, 1415 (1994).
41. Chapman, I. T., Kemp, R. & Ward, D. J. Analysis of high β regimes for DEMO. *Fusion Eng. Des.* **86**, 141–150 (2011).
42. Kim, H.-S. et al. Characteristics of global energy confinement in KSTAR L- and H-mode plasmas. *Nucl. Fusion* **54**, 083012 (2014).
43. Citrin, J. et al. Non-linear stabilization of tokamak microturbulence by fast ions. *Phys. Rev. Lett.* **111**, 155001 (2013).
44. Romanelli, M. et al. Fast ion stabilization of the ion temperature gradient driven modes in the Joint European Torus hybrid-scenario plasmas: a trigger mechanism for internal transport barrier formation. *Plasma Phys. Control. Fusion* **52**, 045007 (2010).

-
- 45. Garcia, J. et al. Key impact of finite-beta and fast ions in core and edge tokamak regions for the transition to advanced scenarios. *Nucl. Fusion* **55**, 053007 (2015).
 - 46. Di Siena, A. et al. New high-confinement regime with fast ions in the core of fusion plasmas. *Phys. Rev. Lett.* **127**, 025002 (2021).
 - 47. Connor, J. W. et al. A review of internal transport barrier physics for steady-state operation of tokamaks. *Nucl. Fusion* **44**, R1–R49 (2004).
 - 48. Peeters, A. G. et al. The non-linear gyro-kinetic flux tube code GKW. *Comput. Phys. Commun.* **180**, 2650 (2009).
 - 49. Bourdelle, C. et al. Impact of the α parameter on the microstability of internal transport barriers. *Nucl. Fusion* **45**, 110 (2005).
 - 50. Candy, J., Belli, E. A. & Bravenec, R. V. A high-accuracy Eulerian gyrokinetic solver for collisional plasmas. *J. Comput. Phys.* **324**, 73–93 (2016).
 - 51. In, Y. et al. Extremely low intrinsic non-axisymmetric field in KSTAR and its implications. *Nucl. Fusion* **55**, 043004 (2015).

Publisher's note Springer Nature remains neutral with regard to jurisdictional claims in published maps and institutional affiliations.

© The Author(s), under exclusive licence to Springer Nature Limited 2022

Article

Methods

KSTAR

KSTAR⁴ is a magnetic fusion device based on the tokamak concept at Korea Institute of Fusion Energy in Daejeon, Republic of Korea (Extended Data Fig. 1). The aim of the KSTAR project is to develop a steady-state-capable advanced superconducting tokamak to establish a scientific and technological basis for ITER and an attractive future fusion reactor. KSTAR is equipped with a fully superconducting magnet system, one of the first tokamaks to feature fully superconducting magnets of great relevance to ITER. The major and the minor radius of KSTAR are 1.8 m and 0.5 m, respectively. The magnetic system consists of 16 niobium–tin direct current toroidal field coils, 10 niobium–tin alternating current poloidal field coils and 4 niobium–titanium alternating current poloidal field coils⁵². The toroidal field strength is up to 3.5 T at the magnetic axis. The two in-vessel cryogenic pumps are located behind the outboard divertor at both the top and bottom sides of the vacuum vessel⁵³. KSTAR is equipped with steady-state heating and current drive systems. NBI is the main heating system with the power up to 6 MW and the beam energy up to 100 keV with a long-pulse capability up to 300 s. Through highly tangential beam geometry, it can provide the highly efficient current and rotation drive required for high-fusion-performance plasmas. The electron cyclotron resonance heating (ECH) system that also plays an important role in high-performance plasma experiments consists of two dual-band devices with a 105/140-GHz and 1-MW-class gyrotron⁵⁴. The KSTAR project plans to obtain more NBI sources and ECH gyrotrons for its heating system⁵⁵.

Diagnostics

Sets of magnetic diagnostic sensors⁵⁶ installed on KSTAR are used to obtain main physics parameters shown in Figs. 1 and 2 and Extended Data Figs. 2 and 5 such as the total plasma current, loop voltage and equilibrium parameters reconstructed by the EFIT code⁵⁷. The magnetic fluctuations drawn in Fig. 1 and Extended Data Fig. 5 are calculated through Fourier transform from the Mirnov coil measurements⁵⁸. The kinetic profiles presented in Fig. 2c and Extended Data Fig. 2b are obtained at the outboard side from Thomson scattering (TS) systems⁵⁹ for the electron temperature and density and from charge-exchange spectroscopy⁶⁰ for the impurity carbon temperature and toroidal rotation velocity. A two-colour interferometer (TCI) with a CO₂ laser and a diode-pumped-solid-state laser⁶¹ and electron cyclotron emission (ECE) measurements are used to determine the electron density and the temperature, respectively, complementary to the TS measurements. The motional Stark effect (MSE) diagnostic⁶² is used to extract the core current density profile for the kinetic equilibrium construction. The neutron emission rate is measured by a uranium-235 fission chamber detector and a helium-3 counter⁶³.

Experimental approach

As aforementioned, the plasma configuration is one of the most important components for accessing FIRE mode. It starts from the limited configuration during the plasma current ramp-up phase. Then, the plasma is detached from the inboard side of the device with the upper single null (USN) configuration. As the plasma is detached from the inboard side, the plasma density is decreased markedly owing to the disconnection of the particle source from the inboard side. The threshold power for the H-mode transition follows the U-shaped curve so that the power for the transition increases as the density decreases below a certain value⁶⁴. Therefore, the lower density from the plasma detachment helps to prevent the H-mode transition. Moreover, it is known that the H-mode transition is difficult for the USN configuration with the ion ∇B drift direction is away from the X-point⁶⁵. By the combination of the effect of the lower plasma density and the USN configuration, the H-mode threshold power becomes higher and the plasma cannot enter the H-mode even with a high heating power. Note that in some

experiments, FIRE mode was obtained even with the lower single null configuration, but the density was kept low, $\approx 10^{19} \text{ m}^{-3}$, to avoid the H-mode transition. In the experiment, an on-axis NBI system called NBI-1, which lies in the horizontal mid-plane of the device, consisting of three positive ion sources, is applied as a main auxiliary heat source⁶⁶. Although the maximum total beam power is about 5.5 MW at the maximum beam energy of 100 keV, less input power, about 4 MW, is injected to avoid H-mode transition while establishing FIRE modes. The ECH system⁶⁷, the other important further heating scheme in KSTAR, is applied mainly to assist the plasma breakdown and to increase the electron temperature while avoiding the H-mode transition. It is noteworthy that FIRE mode can be maintained in the condition of $T_i \approx T_e$ for which some amount of NBI power is replaced with ECH. Extended Data Fig. 2 shows that the ITB structure is sustained with $\beta_N \approx 2.0$ when one NBI source is replaced by ECH, in spite of reduction of the ion heat source. Nonlinear gyrokinetic simulations with the CGYRO code show consistent results that the thermal ion heat flux is substantially reduced with the presence of fast ions even under low $T_i/T_e \approx 0.91$, as shown in Extended Data Fig. 3, which is a relevant temperature ratio in the ITER reference scenario⁶⁸.

Power balance analysis

The integrated tokamak modelling suite, TRIASSIC⁶⁹, incorporating NUBEAM⁷⁰, NCLASS⁷¹ and ASTRA⁷², was used for power balance analysis. The NUBEAM code is a Monte Carlo fast-ion module to compute the power deposition, driven current, momentum transfer, fuelling, fusion reaction and so on by NBI. The NCLASS module calculates the neoclassical transport properties of a multi-species axisymmetric plasma of arbitrary aspect ratio, geometry and collisionality. The ASTRA code solves a set of transport equations in toroidal geometry with various physical modules. In this work, NUBEAM was used to calculate the number density, the energy distribution, and the power deposition of the fast ions produced by NBI, NCLASS was used to calculate the plasma velocity and radial electric field, and ASTRA was used to calculate the plasma transport equations. The effective charge, Z_{eff} , was assumed to be uniform as 1.8 (ref.⁷³) and dominated by carbon owing to lack of measurements. The radiation power loss was neglected. For FIRE mode, shot 22663 was analysed with full measurements mentioned above. For hybrid mode, shot 22658 was analysed with the electron density and temperature profiles from shot 22676, a similar discharge to shot 22658, owing to lack of TS measurements, with the aid of TCI and ECE measurements of shot 22658.

Linear gyrokinetic simulations

The GKW code was used in the linear gyrokinetic analysis for FIRE mode (shot 22663). It simulates microinstabilities and turbulence in a magnetically confined plasma⁴⁸. The most unstable mode of microinstabilities was calculated by GKW for shot 22663 at $\rho = 0.4$ and $t = 5.35 \text{ s}$ with full species assuming carbon impurity with $Z_{\text{eff}} = 1.8$. The profiles and equilibrium of shot 22663 were obtained from the kinetic equilibrium reconstruction with the MSE diagnostics. In the kinetic equilibrium, fast ions whose distributions were calculated by NUBEAM were considered as an independent species with the equivalent temperature⁷⁴. When fast ions were not considered in the analysis, thermal ions, with the thermal ion temperature, replaced them. To fix the contribution of electrons in the scanning of thermal ion density gradients, fast-ion density gradients were modified to satisfy quasi-neutrality. Collisions were considered in all cases. A full geometry with the Hamada coordinate calculated from CHEASE⁷⁵ was used in the GKW simulation.

Nonlinear gyrokinetic simulations

The CGYRO code⁵⁰ was used to perform the nonlinear gyrokinetic analysis for FIRE mode (shot 22663) at the same radial location used in the linear simulations. Through this analysis, we can simulate the transport level induced by turbulence. In these calculations,

geometric effects were considered through the Miller equilibrium model⁷⁶, and rotation effects were also included. The Sugama collision operator⁷⁷ was used to calculate collision effects. Electromagnetic effects were also included in the simulations by calculating the perturbed vector potential parallel to the background magnetic field (δA_{\parallel}) as well as the perturbed electrostatic potential ($\delta\phi$). The ion-scale turbulence ($k_\theta\rho_s < 1$, in which k_θ and ρ_s are the poloidal wavenumber and the sound gyroradius, respectively) was considered in the simulations. Convergence of the simulated heat flux levels on the numerical parameters such as the box size, radial grid number and pitch angle resolution was confirmed.

Analysis of core ITB characteristics

We checked the core ITB characteristics of FIRE mode from four point of views. First, we evaluated whether the inverse-normalized ITG length, R/L_{Ti} is larger than the ITG threshold value. According to the ITG theory^{78–80}, it is hard to increase R/L_{Ti} above the critical value of the ITG onset owing to the induced anomalous transport, so-called stiffness. However, we found that R/L_{Ti} is far above the critical value relaxing stiffness in FIRE mode, as shown in Extended Data Fig. 4c. Second, we checked the time evolution of the ion heat diffusivity calculated from the power balance analysis. As shown in Extended Data Fig. 4a, it was found that the ion heat diffusivity reduces in time correlated with the expansion of ITB although it is still above the neoclassical level (see Extended Data Fig. 4d). Third, we evaluated the relation between the ion energy flux and the ITG to determine whether any bifurcation exists in time and space. As shown in Extended Data Fig. 4e, the normalized ion energy flux draws an S-shaped curve in the three-dimensional (3D) landscape of the flux-gradient space⁸¹. The reduction of the energy flux while the gradient increases implies a transport bifurcation, known to be an ITB characteristic. This bifurcation occurs at $\rho_n \approx 0.3$ where the ITB foot is located when the ITB was thought to be formed. Last, we checked whether the amplitude of electron temperature fluctuations measured by ECE imaging decreases as the ion energy confinement is improved to determine whether the turbulence that persists in the plasma from the breakdown⁸² is reducing. As the ITB location expands to $\rho_n \approx 0.6$, the fluctuation is severely reduced, as shown in Extended Data Fig. 4b, implying stabilization of turbulence. On the basis of the analysis above, an ITB is thought to be formed in the ion energy channel at the core region of FIRE mode owing to stabilization of the ITG turbulence.

Analysis of edge characteristics

Some FIRE modes have plasma edge characteristics similar to that of I-mode^{83,84} in which an ETB is formed only in the energy channel not in the particle channel. It is noteworthy that I-modes are typically obtained with USN configurations with the ion ∇B drift direction away from the X-point, which is similar to the experimental condition of FIRE mode. Therefore, operations of FIRE mode with the USN configuration could have the potential to establish I-mode at the edge with the auxiliary heating power close to the H-mode transition. In I-modes, the edge particle transport remains turbulent owing to the weakly coherent modes, so that the pressure gradient is reduced, and subsequently ELMs are prevented. Similarly, FIRE modes with an I-mode-like edge show a high ITG at the edge region but no clear barrier in the density profile. Therefore, no ELMs are observed, as shown in the D_α signal in Figs. 1f and 2a. Extended Data Fig. 5 presents an example of FIRE mode with an I-mode-like edge, where a weakly coherent mode appears in the Mirnov coil signal. The absence of the particle transport barrier can enhance the fraction of fast ions by reducing thermalization of fast ions with a low density, so as to sustain high performance in FIRE modes. Note that no ITBs seem to be established with the I-mode edge developed in other devices so far.

Statistical analysis of operation window with OD parameters

The stationary operation window is compared for three types of operation regime in terms of the plasma performance (β_N, H_{89}) and the internal inductance (I_i), as shown in Extended Data Fig. 6. One is FIRE modes with the diverted configuration including the I-mode-like as well as the L-mode edge. Another is H-modes with the diverted configuration including hybrid modes. The other is conventional ITB discharges with the L-mode edge at the limited configuration in KSTAR. The plasma internal inductance of FIRE modes is $I_i > 1.25$ higher than that of H-modes, implying more peaked current density profiles with monotonic q -profiles. This is a distinct feature compared with conventional ITB discharges with reversed magnetic shear^{85–87}. High-performance FIRE modes with $\beta_N > 2.0$ and $H_{89} > 2.0$ are located on the relatively low I_i window as a result of the increased bootstrap current due to a broader ITB and/or presence of an I-mode-like structure in the edge region. It is anticipated that FIRE mode can be further enhanced by broadening the ITB and strengthening the ETB with respect to the performance and the bootstrap current fraction.

Data availability

Raw data were generated by the KSTAR team. The data that support the findings of this study are available from the corresponding author upon reasonable request.

52. Kim, K. et al. Status of the KSTAR superconducting magnet system development. *Nucl. Fusion* **45**, 783 (2005).
53. Lee, H. J. et al. Design and fabrication of the KSTAR in-vessel cryo-pump. *Fusion Eng. Des.* **86**, 1993–1996 (2011).
54. Joung, M. et al. Design of ECH launcher for KSTAR advanced Tokamak operation. *Fusion Eng. Des.* **151**, 111395 (2020).
55. Kwak, J.-G. et al. KSTAR status and upgrade plan toward fusion reactor. *IEEE Trans. Plasma Sci.* **48**, 1388–1395 (2020).
56. Lee, S. G. et al. Magnetic diagnostics for the first plasma operation in Korea Superconducting Tokamak Advanced Research. *Rev. Sci. Instrum.* **79**, 10F117 (2008).
57. Lao, L. L. et al. Reconstruction of current profile parameters and plasma shapes in tokamaks. *Nucl. Fusion* **25**, 1611 (1985).
58. Bak, J. G. et al. Initial measurements by using Mirnov coils in the KSTAR machine. in *Proc. of the 37th EPS conference on Plasma Physics* (Ed. C. McKenna) (European Physical Society, 2010).
59. Lee, J. H. et al. Edge profile measurements using Thomson scattering on the KSTAR tokamak. *Rev. Sci. Instrum.* **85**, 11D407 (2014).
60. Ko, W. H. et al. Rotation characteristics during the resonant magnetic perturbation induced edge localized mode suppression on the KSTAR. *Rev. Sci. Instrum.* **85**, 11E413 (2014).
61. Juhn, J.-W. et al. Multi-chord IR-visible two-color interferometer on KSTAR. *Rev. Sci. Instrum.* **92**, 043559 (2021).
62. Chung, J., Ko, J., De Boek, M. F. M. & Jaspers, R. J. E. Instrumentation for a multichord motional Stark effect diagnostic in KSTAR. *Rev. Sci. Instrum.* **85**, 11D827 (2014).
63. England, A. C. et al. Neutron emission from KSTAR ohmically heated plasmas. *Phys. Lett. A* **375**, 3095–3099 (2011).
64. Ahn, J.-W. et al. Confinement and ELM characteristics of H-mode plasmas in KSTAR. *Nucl. Fusion* **52**, 114001 (2012).
65. Carlstrom, T. N. L-H transition and power threshold studies in the DIII-D tokamak. *Fusion Sci. Technol.* **48**, 997–1010 (2005).
66. Jeong, S. H. et al. First neutral beam injection experiments on KSTAR tokamak. *Rev. Sci. Instrum.* **83**, 02B102 (2012).
67. Wang, S. J. et al. Recent experimental results of KSTAR RF heating and current drive. *AIP Conf. Proc.* **1689**, 030014 (2015).
68. Sips, A. C. C. et al. Advanced scenarios for ITER operation. *Plasma Phys. Control. Fusion* **47**, A19 (2005).
69. Lee, C. Y. et al. Development of integrated suite of codes and its validation on KSTAR. *Nucl. Fusion* **61**, 96020 (2021).
70. Pankin, A. et al. The tokamak Monte Carlo fast ion module NUBEAM in the National Transport Code Collaboration library. *Phys. Commun.* **159**, 157 (2004).
71. Houlberg, W. A., Shaing, K. C., Hirshman, S. P. & Zarnstorff, M. C. Bootstrap current and neoclassical transport in tokamaks of arbitrary collisionality and aspect ratio. *Phys. Plasmas* **4**, 3230 (1997).
72. Pereverzev, G. & Yushmanov, P. N. ASTRA Automated System for TRansport Analysis in a Tokamak (IPP, 2002); https://pure.mpg.de/rest/items/item_2138238/component/file_2138237/content
73. Sarwar, S., Na, H. K. & Park, J. M. Effective ion charge (Z_{eff}) measurements and impurity behaviour in KSTAR. *Rev. Sci. Instrum.* **89**, 043504 (2018).
74. Angioni, C. & Peeters, A. G. Gyrokinetic calculations of diffusive and convective transport of particles with a slowing-down distribution function. *Phys. Plasmas* **15**, 052307 (2008).
75. Lutjens, H., Bondeson, A. & Sauter, O. The CHEASE code for toroidal MHD equilibria. *Comput. Phys. Commun.* **97**, 219 (1996).

Article

76. Miller, R. L. et al. Noncircular, finite aspect ratio, local equilibrium model. *Phys. Plasmas* **5**, 973 (1998).
77. Sugama, H., Watanabe, T.-H. & Nunami, M. Linearized model collision operators for multiple ion species plasmas and gyrokinetic entropy balance equations. *Phys. Plasmas* **16**, 112503 (2009).
78. Hahm, T. S. & Tang, W. M. Properties of ion temperature gradient drift instabilities in H-mode plasmas. *Phys. Plasmas* **1**, 1185 (1989).
79. Guo, S. C. & Romanelli, F. The linear threshold of the ion-temperature-gradient-driven mode. *Phys. Plasmas* **5**, 520 (1993).
80. Connor, J. W. & Wilson, H. R. Survey of theories of anomalous transport. *Plasma Phys. Control. Fusion* **36**, 719 (1994).
81. Diamond, P. H. et al. On the dynamics of transition to enhanced confinement of reversed magnetic shear discharges. *Phys. Rev. Lett.* **78**, 1472–1475 (1997).
82. Yoo, M. G. et al. Evidence of a turbulent E_xB mixing avalanche mechanism of gas breakdown in strongly magnetized systems. *Nat. Commun.* **9**, 3523 (2018).
83. McDermott, R. M. et al. Edge radial electric field structure and its connections to H-mode confinement in Alcator C-Mod plasmas. *Phys. Plasmas* **16**, 056103 (2009).
84. Liu, Z. X. et al. The physics mechanisms of the weakly coherent mode in the Alcator C-Mod Tokamak. *Phys. Plasmas* **23**, 120703 (2016).
85. Levinton, F. M. et al. Improved confinement with reversed magnetic shear in TFTR. *Phys. Rev. Lett.* **75**, 4417 (1995).
86. Strait, E. J. et al. Enhanced confinement and stability in DIII-D discharges with reversed magnetic shear. *Phys. Rev. Lett.* **75**, 4421 (1995).
87. Fujita, T. et al. Plasma equilibrium and confinement in a tokamak with nearly zero central current density in JT-60U. *Phys. Rev. Lett.* **87**, 245001 (2001).

Acknowledgements We express our gratitude to R. Nazikian at Princeton Plasma Physics Laboratory, H. Zohm at Max-Plank-Institute for Plasma Physics, W. Choe at Korea Advanced Institute of Science and Technology and J. Candy and E. Belli at General Atomics for fruitful discussions. We also thank all members of the KSTAR centre for their support and assistance in our studies. This work was supported by the Ministry of Science and ICT under the Korea Institute of Fusion Energy R&D Program KSTAR Experimental Collaboration and Fusion Plasma Research (KFE-EN2101-12), the National R&D Program through the National Research Foundation of Korea (NRF) funded by the Korea government (Ministry of Science and ICT) (NRF-2021M1A7A4091135), and the National Supercomputing Center with supercomputing

resources including technical support (KSC-2020-CRE-0364) and by the US Department of Energy under contract number DE-AC02-09CH11466 (Princeton Plasma Physics Laboratory). We gratefully acknowledge The Research Institute of Energy and Resources and The Institute of Engineering Research at Seoul National University.

Author contributions Y.-S.N., H.H., J.C., Y.H.L., S.J.P. and Y.S.P. conceived the experiments in KSTAR. H.H., J.C., J.Kang, S.H.H., S.J.P., Y.H.L. and Y.-S.N. conducted all the experiments in KSTAR. J.G.B. diagnosed the magnetic perturbations in the experiments using the Mirnov coil measurements. W.H.K. and J.K.L. diagnosed the ion temperature in the experiments using charge-exchange spectroscopy. J.H.Lee (Korea Institute of Fusion Energy and Korean University of Science and Technology) diagnosed the plasma electron and density profiles using TS. K.D.L. diagnosed the electron temperature in the experiments using the ECE. J.Ko diagnosed the radial magnetic pitch angle profile using the MSE. J.J. measured the emission lines from neutralization of ion species to diagnose the impurity intensity as well as the plasma interaction. K.C.L. diagnosed the plasma density using the TCI. J.H.K. diagnosed and analysed the fast-ion properties. M.J.C. and J.H.Lee (Korea Institute of Fusion Energy) diagnosed the temperature fluctuation using the ECE imaging. S.J.P., Y.H.L., C.Y.L. and G.J.C. performed the power balance and the linear gyrokinetic simulations. C.S. performed the nonlinear gyrokinetic simulations and investigated the impacts of fast ions on energy transport through these simulations. T.S.H., J.P.L., C.S., G.J.C., S.M.Y., S.K.K. and Y.-S.N. analysed the simulation results. H.H, S.J.P., J.-K.P., J.S., B.K., J.G., M.S.C., C.S. and Y.-S.N. prepared the manuscript, figures and video. W.C.K. and S.W.Y. supported all of this work as the KSTAR project managers. Y.-S.N. designed and led the whole research including coining the new confinement regime as FIRE mode. All authors analysed the results and contributed to the compilation and review of the manuscript.

Competing interests The authors declare no competing interests.

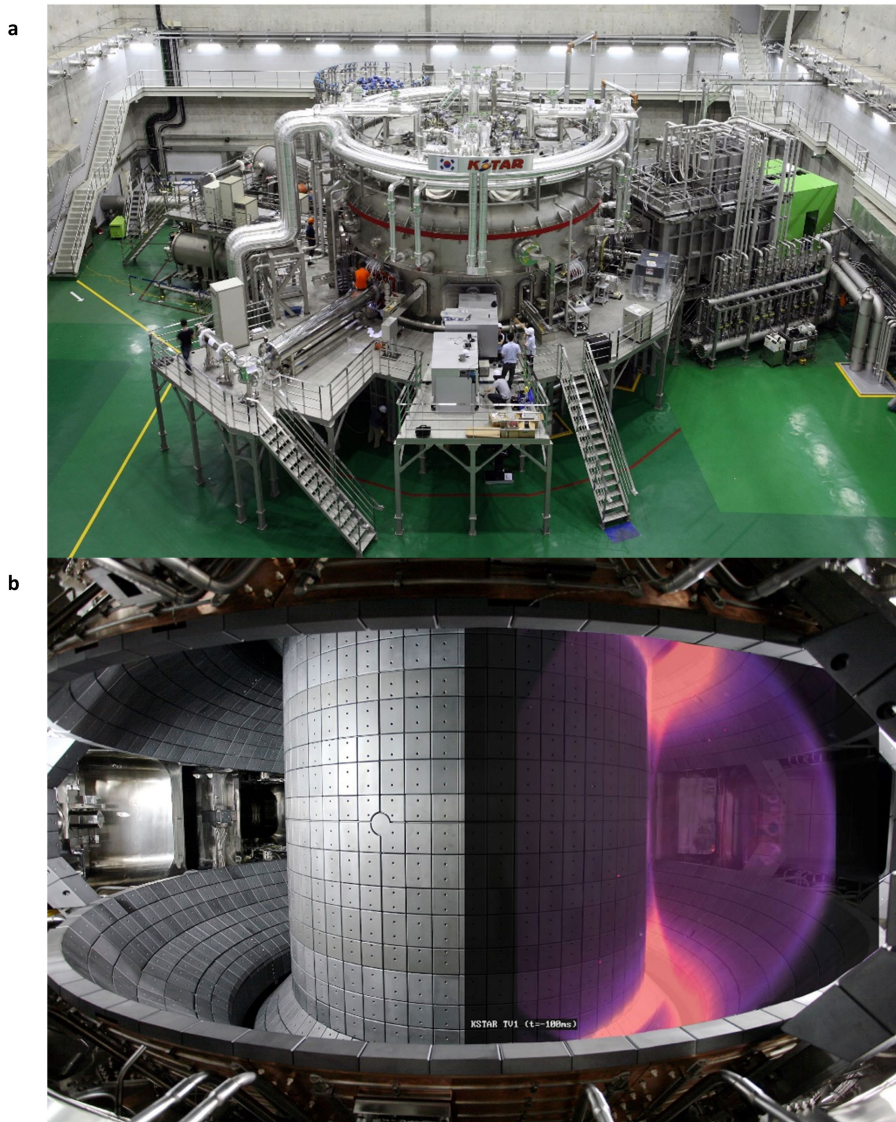
Additional information

Supplementary information The online version contains supplementary material available at <https://doi.org/10.1038/s41586-022-05008-1>.

Correspondence and requests for materials should be addressed to Y.-S. Na.

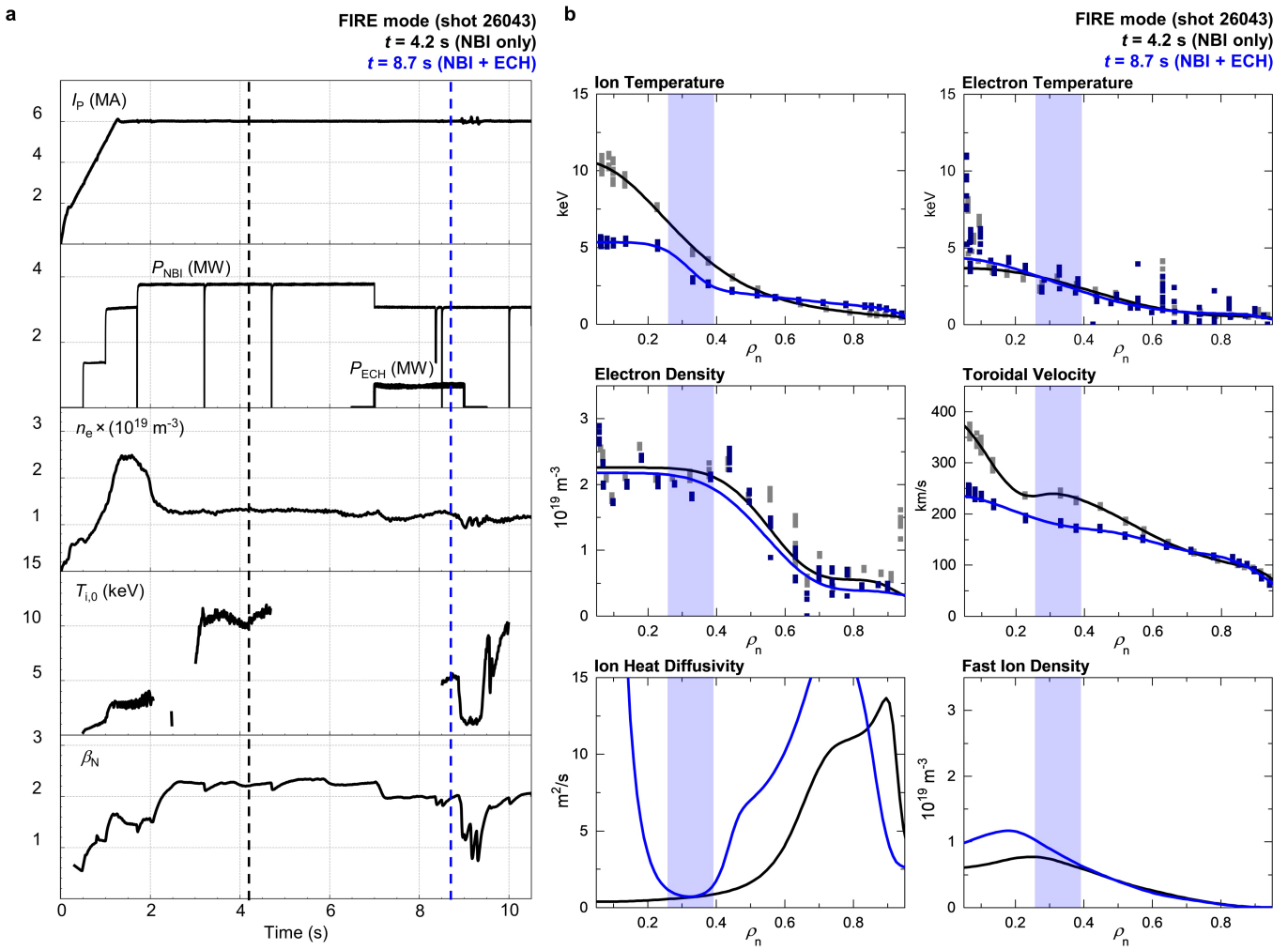
Peer review information *Nature* thanks Hartmut Zohm and the other, anonymous, reviewer(s) for their contribution to the peer review of this work.

Reprints and permissions information is available at <http://www.nature.com/reprints>.



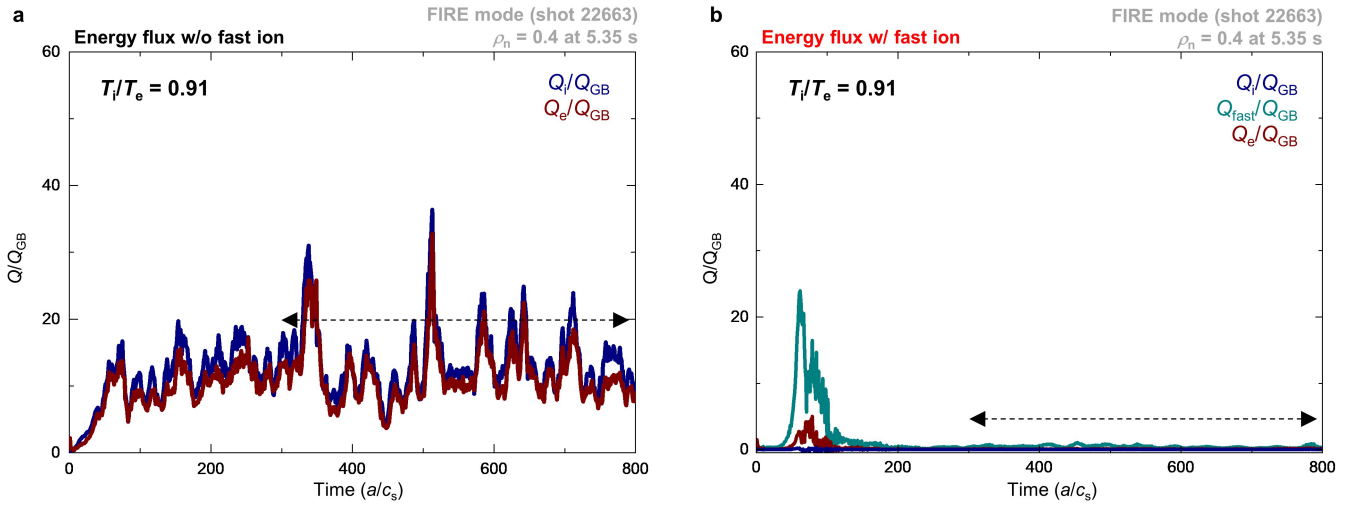
Extended Data Fig. 1 | External and internal view of the KSTAR device. a, The Korean Superconducting Tokamak Advanced Research (KSTAR) device at KFE, Daejeon, Republic of Korea. **b,** Plasma composite image of the KSTAR vacuum vessel.

Article



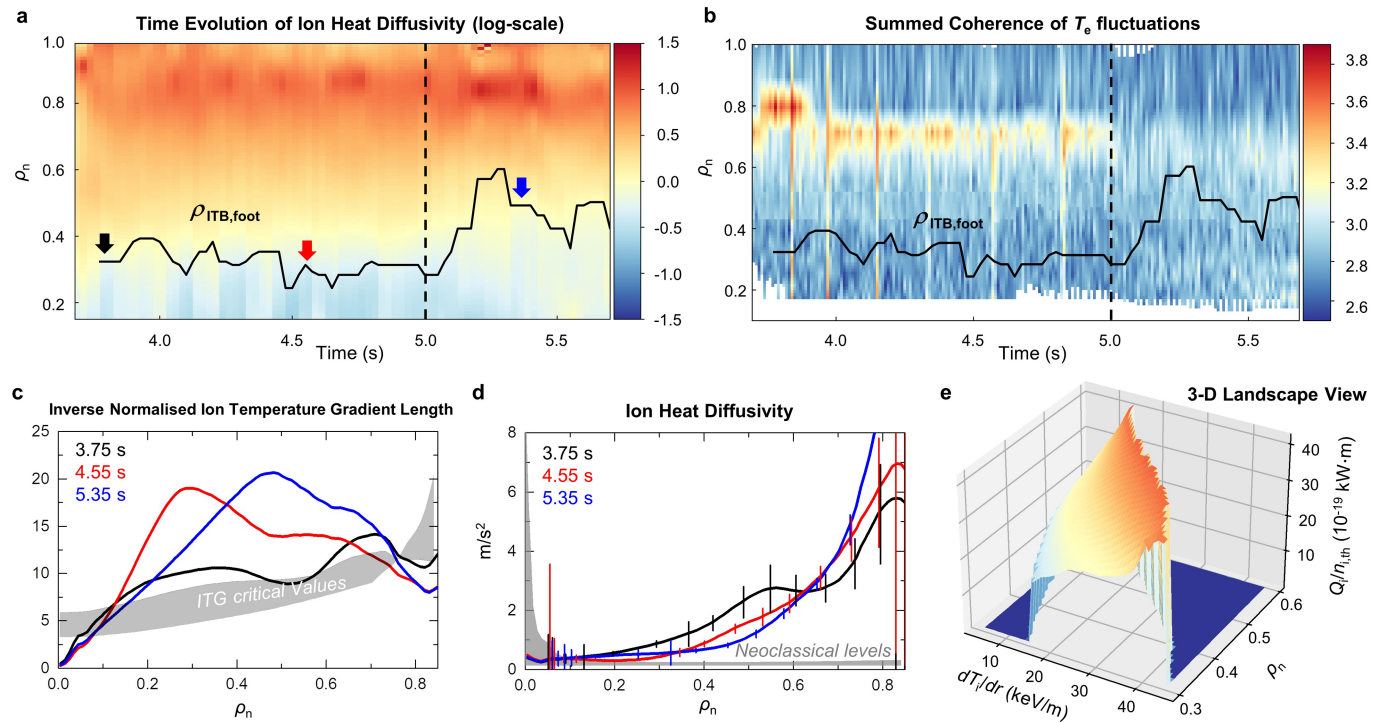
Extended Data Fig. 2 | Comparison between an NBI only and an ECH applied FIRE mode. **a**, Overview of an ECH injected FIRE mode (shot 26043). **b**, The ion temperature, electron temperature, electron density, toroidal rotation velocity, ion heat diffusivity, and fast ion density profiles in ρ_n at 4.2 s (NBI only) and 8.7 s (NBI+ECH). The fast ion density profiles calculated by the NUBEAM

code and the ion heat diffusivity profiles calculated from the power balance analysis with TRIASSIC incorporating NUBEAM, NCLASS, and ASTRA. The blue shaded region indicates the region of the ITB from the foot to the shoulder while ECH was applied.



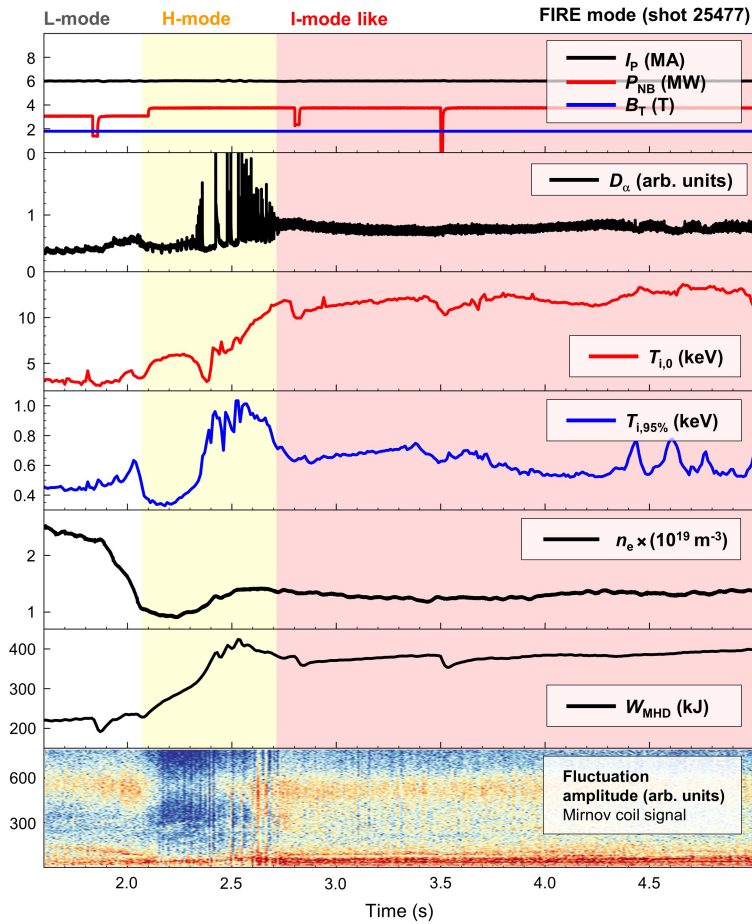
Extended Data Fig. 3 | Nonlinear gyrokinetic simulation results with the CGYRO code in the case of $T_i/T_e \sim 0.91$. **a**, The energy fluxes without considering the fast ions versus the simulated time, **b**, the energy fluxes with considering the fast ions versus the simulated time. Each energy flux of thermal ions (Q_i), fast ions (Q_{fast}), and electrons (Q_e) normalised to the gyro-Bohm energy flux (Q_{GB}) is coloured by navy, dark cyan, and wine,

respectively. Here, the simulation setup and the notations are the same as those used in Fig. 4c and d except the T_i/T_e ratio - 0.91, where the experimental T_i/T_e ratio is 1.42. Note that only latter part of the nonlinear simulation results, indicated by the arrow double end line, should be considered since a certain simulation time requires until the simulated turbulence is saturated by nonlinear effects.



Extended Data Fig. 4 | ITB characteristics of a FIRE mode (KSTAR Shot 22663). **a**, The time evolution of the thermal ion heat diffusivity in ρ_n calculated from the power balance analysis with TRIASSIC incorporating NUBEAM, NCLASS, and ASTRA. $\rho_{ITB,foot}$ is plotted in the black line to show the time evolution of the ITB region. **b**, Fluctuation of the electron temperature measured by Electron Cyclotron Emission Imaging (ECEI) for ITB characteristics of a FIRE mode (Shot 22663). The coherence between poloidally adjacent channels near $Z=0$ m is summed over frequency 0–250 kHz to represent the amplitude of turbulence, where Z is the vertical position of an ECEI channel. As ITB expands outwards to $\rho_n \sim 0.6$, the edge fluctuations are significantly reduced. The black dashed line indicates the NBI heating timing.

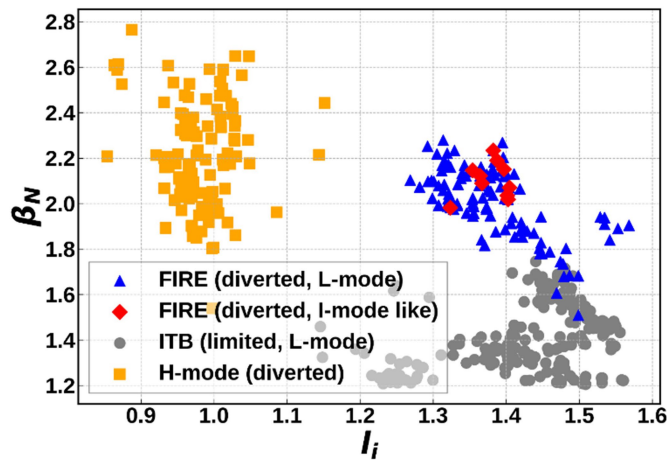
c, the inverse normalised ion temperature gradient length profile, **d**, the thermal ion heat diffusivity profile calculated from the power balance analysis at 3.75 s, 4.55 s, and 5.35 s. The black, red, and blue curves correspond to the time points indicated by arrows in **a**. The error bars are estimated from standard deviation of ion temperature diagnosed by Charge Exchange Spectroscopy (CES) for each channel. **e**, 3-D landscape view for ITB characteristics of a FIRE mode (shot 22663). The normalised ion energy flux to the thermal ion density versus the ion temperature gradient is plotted at $\rho_n = 0.3, 0.4, 0.5$, and 0.6 from 3.7 s to 5.7 s. The transport bifurcation occurs at $\rho_n \sim 0.3$ where the ITB foot locates when the ITB was formed.



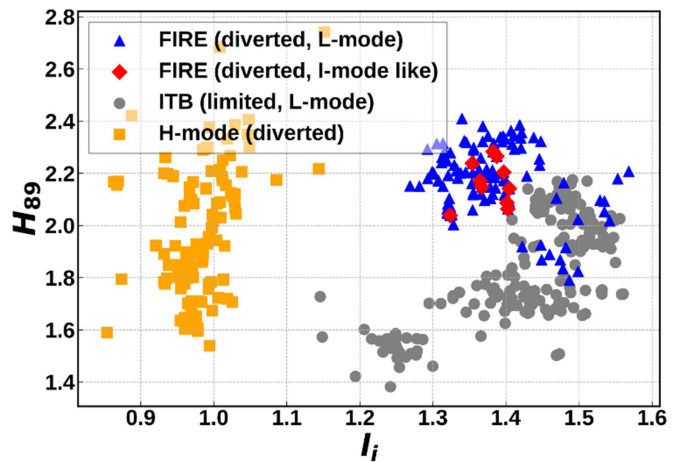
Extended Data Fig. 5 | The time evolution of main parameters of a FIRE mode (KSTAR Shot 25477) during the transition from L-mode to an I-mode like via H-mode. The plasma is in L-mode, H-mode including the dithering phase, and I-mode like phase up to 2.0 s, 2.1 s to 2.7 s, and after 2.7 s, respectively. A strong

weakly coherent modes are observed in the I-mode like phase in the magnetic fluctuation detected by Mirnov coils. The ion temperature close to the edge ($T_{i,95\%}$) in the I-mode like phase is higher compared with the L-mode phase which could imply the formation of an ETB.

Article



Extended Data Fig. 6 | The stationary operation window in terms of the normalised plasma pressure to the magnetic pressure β_N and confinement enhancement factor H_{89} versus internal inductance I_i . They are calculated with magnetic EFIT. Yellow squares present H-modes at the divertor configuration including hybrid modes. Grey circles are conventional ITB



discharges with the L-mode edge at the limited configuration and blue triangles are FIRE modes with the L-mode edge at the diverted configuration. Red diamonds present FIRE modes with the I-mode like edge at the diverted configuration.